ENHANCEMENT OF HYDROCARBON PHASE DIAGRAM GENERATION USING MICROFLUIDIC CHAMBERS

A Thesis

by

GABRIEL RAY SIEGEL

Submitted to the Office of Graduate and Professional Studies of
Texas A&M University
in partial fulfillment of the requirements for the degree of

MASTER OF SCIENCE

Chair of Committee,	Hadi Nasrabadi
Co-Chair of Committee,	Debjyoti Banerjee
Committee Member,	Sara Abedi
Head of Department,	Jeff Spath

May 2020

Major Subject: Petroleum Engineering

ABSTRACT

Understanding the phase behavior of hydrocarbons is essential in the oil and gas industry. However, current methodologies for obtaining phase diagrams are time-consuming, expensive, and yield few data points. Thus, a new methodology for generating phase diagrams is required.

In this work, a novel experimental methodology is presented for generating phase diagrams utilizing microfluidics. The designed microfluidic device utilizes a multiplexed network of dead-end chambers to generate 1,000 constant composition expansion data points over 100 temperature steps and 10 pressure steps. From these data points, phase transitions can be plotted, thus creating a phase diagram.

The methodology for fabricating silicon-glass microfluidic devices presented produces a microfluidic device that is capable of withstanding pressures up to 1,000 psi. This pressure limit is sufficient for most hydrocarbon phase diagram generation. The methodology can serve as a guide for the fabrication of silicon-glass microfluidic devices.

Using the fabricated device, a phase diagram is generated for n-butane. The results demonstrate the device's capability to produce accurate data and generate a phase diagram that is within 0.50% of simulated results.

ACKNOWLEDGEMENTS

I would like to thank my committee chair, Dr. Nasrabadi, for his support and guidance over the course of this research. I would also like to thank my committee members, Dr. Abedi and Dr. Banerjee, for their time and assistance while serving on my committee.

I would like to thank my research colleagues, Mehrdad Alfi and Qi Yang, for providing me with assistance with regards to conducting and setting up the experimentation. I would like to also thank the staff at the Aggiefab for assisting with the training and equipment maintenance that were required to fabricate the devices.

I would like to thank my parents and family for their support throughout this program. I would also like to thank my brother, Harry, for his assistance with regards to machining and engineering drawings.

Lastly, I would like to thank Chateau Schwift and the Schwifty Gang for making this Master's program an enjoyable time and great experience. Without them, I probably would have finished this degree on time.

CONTRIBUTORS AND FUNDING SOURCES

Contributors

This work was supported by a thesis committee consisting of Professor Hadi Nasrabadi [advisor] and Professor Sara Abedi of the Department of Petroleum Engineering and Professor Debjyoti Banerjee of the Department of Mechanical Engineering.

All work conducted for the thesis was completed by the student independently.

Funding Sources

Graduate study was supported by a fellowship from Texas A&M University and Marathon Oil Company.

NOMENCLATURE

CCE	Constant Composition Expansion
EOS	Equation of State
P-T	Pressure-Temperature
PECVD	Plasma-Enhanced Chemical Vapor Deposition
PVT	Pressure, Volume, Temperature
RIE	Reactive Ion Etching

TABLE OF CONTENTS

Page

LIST OF FIGURES

Page

LIST OF TABLES

Page

1. INTRODUCTION

1.1. Background

Some of the most important information in the oil and gas industry comes from the understanding of the fluid phase behavior. This knowledge provides a general description of the fluid properties that are necessary throughout the life of a field (Firoozabadi 1999).

Phase behavior is described as the conditions of temperature and pressure for which different phases of a fluid can exist (McCain 1990). Fluid phase behavior is described through a phase diagram (or pressure-temperature (P-T) diagram). The phase diagram displays the boundaries of pressure and temperature under which the various phases of a substance will be present.

Reservoir fluid properties are obtained through a series of experiments that manipulate 3 variables, pressure, volume, and temperature (PVT). Constant composition expansion (CCE) experiments are used for the generation of phase diagrams. These experiments are conducted using a PVT Cell in which a known mass of reservoir fluid is placed. The temperature is kept constant and the pressure is slowly lowered from reservoir pressure, and the volume is recorded at each pressure step (Whitson and Brule 2000).

Though CCE experiments in PVT cells are the industry standard, the experiments can be time-consuming and expensive (Di Primio et al. 1998). There is thus a need for an update to the practice of generating hydrocarbon phase diagrams.

1.2. Microfluidics Development and Expansion

Microfluidics consists of experimental techniques that utilize micro-fabricated structures for fluid handling. These structures contain cross section dimensions less than 500 μm, which results in small volume capacities (Nge et al. 2013). Microfluidic devices offer many useful capabilities including the ability to utilize very small quantities of samples and to carry out experimentations with high resolution and sensitivity. This, in turn, leads to a lower cost, shorter time of analysis, and smaller footprint for the experimental device (Whitesides 2006).

The early applications of microfluidic technologies were used for micro-analytical methodologies. Terry et al. (1979) applied microfluidics through the use of a fabricated silicon wafer to conduct gas-phase chromatography. Their design lead to a significant reduction in the time to conduct the chromatographic measurements when compared with the conventional techniques at the time. Though the work conducted showed the ability of microfluidic technologies to greatly improve analytical methodologies, microfluidics did not see further use and development until over a decade later, when use of the devices gained much popularity. During this time, the use of microfluidics branched across many different fields which led to a greater diversification in fabrication materials and techniques (Reyes et al. 2002).

The application of microfluidics in different industries and areas of research has shown the great benefits of the technique. Manz et al. (1990) showed that the use of microfluidic techniques could be applied to chemical monitoring experimentation to create miniaturized total chemical analysis systems. The microfluidic devices created allowed

for faster and more efficient chemical sensing while consuming less materials and allowing multiple measurements to be conducted simultaneously. In the field of genomics, microfluidic based microsystems have a proven record of improving DNA experimentation (Marshall and Hodgson 1998). Sanders and Manz (2000) showed that microfluidic systems were improving the rate of experimentation by orders of magnitudes at the time. Reedy et al. (2010) developed a microfluidic device for the purification of nucleic acids from biological samples displaying the ability of combining two solid-phase extraction processes on the one device. Mora et al (2011) developed a completely automated microfluidic device using an array of pneumatically actuated valves and pumps with the capability to conduct biological and chemical analyses for remote operation during space exploration. More recently, Ma et al. (2017) indicated that microfluidic systems are improving the newer experimental technique of next-generation sequencing by increasing the test rate and significantly improving the data quality for single cell studies.

Though the origin of microfluidic application started with chemical and biological experimentation, the technique continues to expand across many different fields of engineering and science. Nguyen et al. (2019) estimate that the rapid growth of interest in microfluidic devices will continue and soon reach a $6 billion (U.S.) market. This metric indicates the current and future importance of microfluidics and lab-on-a-chip experimentation.

1.3. Application of Microfluidics in the Oil and Gas Industry

Microfluidic experimental methods have been gaining interest in the oil and gas industry. Microfluidics provides the oil and gas industry with the opportunities of providing information on sub-surface operations (fluid transport, pore network models, etc) and enhancing current fluid property analysis techniques (Sinton 2014).

1.3.1. Microfluidics for Fluid Transport and Pore Network Models

Microfluidic pore-scale resolution networks, known as micromodels, are a form of microfluidic research that have been used to investigate transport phenomena for oil and gas research (Günther and Jensen 2006). Predating the advent of modern microfluidics, Bonnet and Lenormand (1977) first constructed a microfluidic network using photoresist processes associated with the future microfluidic fabrication procedures to observe the displacement of the meniscus formed by two phases under different conditions. Oren and Pinczewski (1995) constructed two-dimensional glass micromodels to conduct three-phase (gas-oil-water) displacement experiments under strongly water wet and strongly oil wet conditions. For their fluid transport study, Berejnov et al. (2008) represented the porous medium as a structured microfluidic network tunable surface properties. This allowed for the investigation of capillary capillarity effects independent of fluid properties and network geometry.

Micromodels have also been used to investigate flooding processes. Sohrabi et al. (2008) developed a high-pressure micromodel pore network to visualize water-alternating gas injection displacement mechanisms. Similarly, Meybodi et al. (2011) utilized glass micromodels to investigate the performance of water and polymer flood processes through

a simple pore network. Buchgraber et al. (2011) utilized an SEM image of a sandstone to generate a pore network for conducting polymer flood displacement tests with a glass micromodel. In their pore network micromodel, Gunda et al. (2011) utilized modern microfluidics to construct micromodels of porous media based on advance microscopy scans of a core sample, thus creating what they term as a 'Reservoir-on-a-Chip'. This microfluidic approach resulted in similar oil-displacement patterns as obtained in core-scale flooding experiments, proving the viability of the methodology.

1.3.2. Microfluidics for Enhanced Oil Recovery

Similar micromodels have been utilized for investigation of enhanced oil recovery (EOR) techniques (Lifton 2016). The main areas of EOR that have been investigated using microfluidics include microbial EOR and heavy oil extraction.

Microbial EOR is one area of enhanced recovery that has been investigated using microfluidics. Armstrong and Wildenschild (2012) developed a pore-scale micromodel to investigate the mechanisms of microbial EOR. Visualization through microfluidics allowed for the explanation of the effectiveness of the EOR process by capillary number effects. Khajepour et al. (2014) utilized a micromodel to study microbial EOR, particularly the mechanisms of altering wettability and relative permeability. The microfluidic approach allowed for the visualization of fluid distributions and resulted in the conclusion that the process alters the relative permeability between oil and water, thus improving the recovery efficiency.

The next area of EOR investigated through the use of microfluidics are heavy oil extraction processes. Bowden et al. (2010) utilized a micro-bead pack injected in a glass

micromodel to simulate a porous medium for investigating different methods of EOR for heavy oils, attributing the enhancement in the oil recovery to the alteration in wetting behavior and reduction in oil viscosity. De Haas et al. (2013) created a micromodel to simulate the thermal oil recovery process of steam assisted gravity drainage. Through the use of their micromodel pore network, they compared the use of a steam containing alkaline additives versus pure steam and were able to visually quantify the size of the emulsions created as well as measure the drainage rates with the two fluids.

1.4. Application of Microfluidics for Oil and Gas PVT Studies

Since fluid properties in microfluidic devices are similar to bulk systems, and microfluidic devices provide many experimental benefits (rapid heat and mass transfer, access for visualization, and precise control of temperatures, pressures, and compositions, etc.), microfluidic experimental methods are particularly well suited for performing phase behavior analyses for the oil and gas industry (Bao et al. 2017). When conducting PVT experimentation, the use of high pressures and temperatures is expected, however, common microfluidic devices cannot withstand these conditions. Marre et al. (2010) developed a methodology for the successful design and use of high pressure and temperature microfluidic systems using a silicon-glass based construction. The designed system could withstand pressures and temperatures up to 30 MPa and 400 °C (4,350 psi and 750 °F, respectively). This fabrication methodology has become the norm for microfluidic PVT systems.

1.4.1. Microfluidics for Fluid Analysis Studies

Microfluidics has been applied for understanding many fluid phase phenomena. This includes mass transfer, diffusivity, miscibility, and precipitation. Luther et al. (2013) investigated mass transfer in multiphase mixtures composed of oil, water, and CO_2 using a microfluidic device, proving the viability of the methodology for characterizing and quantifying of key parameters that influence mass transfer. Fadaei et al. (2011) accurately measured diffusion coefficients of CO_2 in bitumen utilizing a microfluidic device. Fadaei et al. (2013) also measured toluene-bitumen diffusivity using a microfluidic approach combined with bright field microscopy. Nguyen et al. (2015) utilized microfluidics to obtain a rapid measurement of minimum miscibility pressure of CO_2 in crude oil samples. This approach resulted in a highly accurate measurement of minimum miscibility pressure in a much shorter time than the conventional methodology. Bowden et al. (2009) developed a microfluidic approach for measuring asphaltene content and precipitation for heavy oil samples. Molla et al. (2016) measured wax appearance temperature of reservoir fluids with a reusable microfluidic device.

1.4.2. Microfluidics for Nano-Scale PVT Studies

With the growth of unconventional oil and gas resources, there has been an increased interest in understanding phase behavior of hydrocarbons at the nanoscale using molecular simulation and microfluidic techniques (Jin and Firoozabadi 2015). Within these unconventional hydrocarbon systems, the majority of the hydrocarbons reside in pores within the nanometer scale (Kuila and Prasad 2013). Luo et al. (2017) utilized a pore-size dependent equation of state (EOS) to model the confinement effect on

hydrocarbons within nanopores, demonstrating the loss of oil recovery within nanopores due to a difference in phase behavior, when compared to the bulk region, as pressure depletes. Jin et al. (2017) used molecular simulation to show that the decrease in pore diameter to the sub 10 nm range lead to a greater divergence in phase behavior for methane from that observed under bulk conditions.

Though molecular simulations are a useful tool, there is still a necessity to validate the results through experimentation using micro/nanofluidics. Luo et al. (2016) utilized controlled-pore glasses with pore sizes of 4.3 and 38.1 nm along with differential scanning calorimetry to experimentally observe the effect confinement has on the bubble points of octane and decane. Luo et al. (2018) continued this work to study the effect the nanopores had on the phase behavior of hydrocarbon mixtures, noticing a deviation from the bubble point within the 4.3 nm pore. Wang et al. (2014) conducted a preliminary study on the effect of nanoconfinement on hydrocarbon phase behavior. The study utilized pure pentane on a microfluidic and nanofluidic device and realized that vaporization of the liquid phase was suppressed within the nanochannels when compared to that of the microchannels. Parsa et al. (2015) utilized the same design to investigate the condensation of pentane under nanoconfinement, finding that the condensation pressure was lowered in channel depths under 50nm. Alfi et al. (2016b) utilized a similar nanochannel design on a microfluidic device to investigate the confinement effect on hydrocarbon phase behavior. Results showed that the confinement effect on the bubble point in 50nm channels was negligible and capillary-pressure-based models fail to predict the phase behavior under confinement. Alfi et al. (2017) continued this work by

investigating the bubble point temperature shift of hydrocarbon mixtures under confinement, observing a shift in phase behavior in pore sizes of 10 nm. Alfi et al. (2016a) utilized the same device to study the nanoconfinement effect on gas-liquid contact angles at shallower depths of 10 nm. Yang et al. (2019) conducted a visualization study on the effect of sub-10 nm slit pores on the dew point pressure of n-butane. The study showed a deviation due to confinement effects, and confirmed the observations with molecular simulations.

1.4.3. Microfluidics for Phase Behavior Studies

The phase behavior of hydrocarbons are of particular interest in the oil and gas sector. Microfluidics has been applied for detecting the bubble point and dew point of hydrocarbon systems, as well as for generating P-T diagrams.

Mostowfi et al. (2012) developed the first microfluidic PVT system capable of detecting the bubble point of multi-component hydrocarbons. The device was fabricated using standard silicon lithography, reactive ion etching (RIE), and anodic bonding. The design of the device simulated the phase transition of a reservoir fluid as it travels through the wellbore from the formation to the surface, allowing for the measurement of the bubble point of multicomponent hydrocarbons in a fraction of the time required for conventional PVT measurements.

Pinho et al. (2014) investigated the thermodynamics of multicomponent fluid samples at high pressures and temperatures using a microfluidic approach. Measurements of dew points and bubble points were conducted by varying temperature under isobaric conditions using optical detection. The P-T diagram was then constructed by connecting

the measured dew points and bubble points. The results were accurate to simulated and literature data and obtained around 5 times faster when compared to conventional methodologies.

Microfluidics has been utilized in studies of fluid phase equilibria. Togo et al. (2013) utilized a microfluidic system to shorten measurement times when conducting vapor-liquid and liquid-liquid equilibria for mixtures of water and aromatic hydrocarbons. Luther et al. (2015) combined a microfluidic system consisting of a micro-capillary with selective Raman spectroscopy to non-invasively characterize vapor-liquid equilibria in multiphase flows for binary and ternary mixtures of aromatic hydrocarbons, water, carbon dioxide or nitrogen. Sullivan and Angelescu (2016) developed a microfluidic device capable of measuring the bubble point pressures of liquids using short thermal pulses and observing the nucleation of bubbles using microscopy.

The use of multiplexing has recently been applied to generate full P-T phase diagrams. Bao et al. (2016) created a microfluidic device that demonstrated the capability of generating a full P-T phase diagram in a single run for pure CO2 and a CO2-N mixture. The device utilized 100 rows of 100 micro-wells connected by a resistor channel to apply a pressure gradient from inlet to outlet and an external heater and chiller placed on the device to apply a temperature gradient. This generated 10,000 simultaneous measurements at different pressure and temperature conditions in a single run. Xu et al. (2017) utilized a similar concept to develop a microfluidic device to generate a full P-T phase diagram in a single run for a methane-propane mixture. The design implemented multiplexing to connect 10 rows of 100 micro-chambers by a resistor channel to apply a

pressure gradient from inlet to outlet and a similar arrangement for applying a temperature gradient. This generated 1,000 simultaneous measurements at different P-T conditions in a single run. The design of the micro-chambers simulated a single point of data in a CCE experiment. The multiplexing designs utilized decreased the experimentation time by two orders of magnitude and provided accurate results compared to simulation.

1.5. Research Objectives

The objectives of the research are as follows:

- To *provide* a methodology for the fabrication of silicon-glass microfluidic and nanofluidic devices for PVT experimentation.
- To *provide* an experimental procedure for generating PVT data from the utilized microfluidic device.
- To *generate* a P-T diagram for a single component hydrocarbon, demonstrating the capabilities of the microfluidic device.

2. METHODOLOGY

2.1. Microfluidic Device Design

The sealed microfluidic device (referred to as a "chip") used was designed to allow for simultaneous conducting of up to 1,000 Constant Composition Expansion (CCE) tests, similar to the design used by Xu et al. (2017). This functions by having 10 interconnected rows with each row having 100 dead end chambers. Each chamber is 100 µm in width and 2 mm in length. The chamber network will be etched to over 10 µm in depth to avoid confinement effects. A temperature gradient is applied across the rows using an external heating block, and a pressure gradient is applied from inlet to outlet down each row through the use of a pressurizing fluid. This allows for 1,000 CCE tests to be conducted at 10 different pressures and 100 different temperatures simultaneously. A schematic of the design can be viewed in **Figure 2.1**.

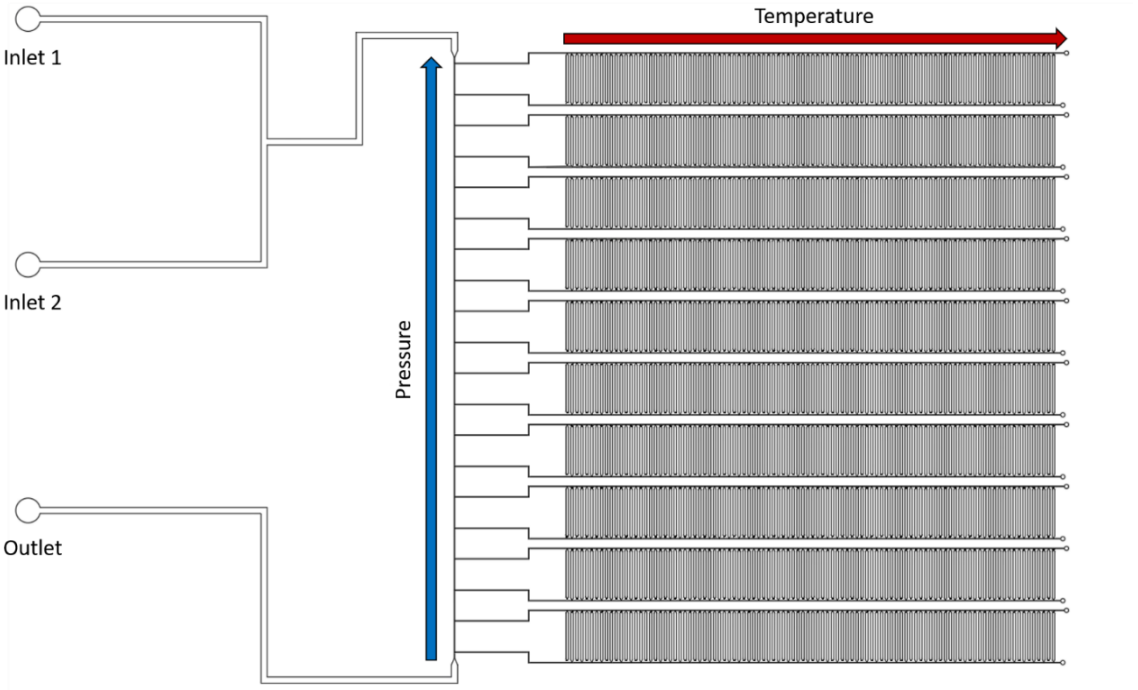

Figure 2.1 – Schematic of the Microfluidic Device Design Illustrating the Pressure and Temperature Gradients Applied.

2.2. Microfluidic Device Fabrication

Top-down micro/nanofabrication techniques were used to create the microfluidic chips used for experimentation. This microfluidic fabrication technique was selected due to its allowance of good control of the size and distribution of features (Gale et al. 2018). The fabrication process was conducted at the AggieFab Nanofabrication Facility and consisted of a multi-step procedure following recommendations from the staff at the facility and literature.

The process consists of four main steps. The first step consists of preparation of the silicon wafer for etching. The second step consists of etching the pattern into the silicon wafer. The third step consists of drilling of the wafer for fluid injection purposes,

and the final step consists of bonding a borosilicate glass wafer to the fabricated wafer to seal the device.

The first step of the preparation process was to clean a single crystal silicon wafer ({100} p-type). The next step was to deposit a thin film of silicon-dioxide (SiO_2) using plasma-enhanced chemical vapor deposition (PECVD) on an Oxford Plasmalab 80 PECVD (Metzler and Patel 2017). The recipe used is shown in Table 2.1. This serves as a protective layer during the selective silicon (Si) etching that is required to reach the desired channel depths and also aids in the bonding process. Thickness of the deposited SiO_2 layer was confirmed using an Ocean Optics NanoCalc DUV Spectroscopic Thin Film Measurement system. The next step required was to coat the wafer with a layer of photoresist (AZ5214) using a spin coater and a hot plate for applying and baking the photoresist onto the wafer (Keck Microfabrication Facility 2002). The function of the photoresist is to provide protection to the areas that are not desired to be etched during the selective SiO_2 etching process. The photoresist coated wafer can now be patterned with the design that will be etched into the wafer. To pattern the wafer, photolithography was used. This technique allows for the creation of accurate feature sizes down to 1 micron (Harriott 2000). The patterning process was conducted using an EVG 610 Double-sided Mask Aligner and a chrome mask was used to pattern the wafer. The chrome mask was purchased with the intended design from an external company (Photomask Portal). The equipment aligns the chrome mask above the wafer and then emits an ultraviolet (UV) light that passes through the exposed areas in the chrome mask. The UV light alters the photoresist in the areas exposed and allows for removal of the photoresist in the areas that

will be etched. The altered photoresist was removed using a developer solution (AZ726) which leaves the photoresist intact in areas that will not be etched. The patterned wafer was then baked again to increase the resistance of the photoresist to the upcoming etching process. **Figure 2.2** displays a diagram of the steps taken to prepare the chip for etching.

Table 2.1 - Deposition Parameter Values for PECVD of SiO_2.

Deposition Parameter	Value	Units	Deposition Parameter	Value	Units
Temperature	350	(Celsius)	**SiH_4**	425	(SCCM)
Pressure	1000	(milliTorr)	**N_2O**	710	(SCCM)
Forward Power	20	(Watts)	**Deposition Rate**	~47.4	(nm/min)

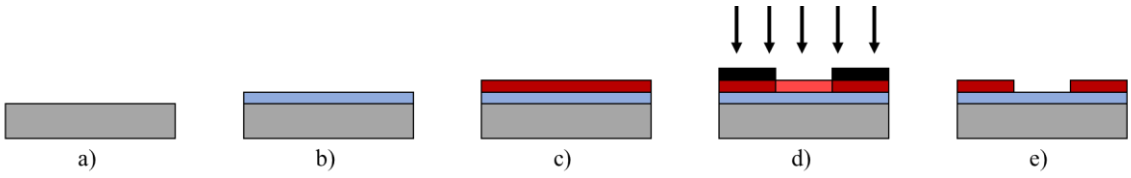

a) Process starts with a clean Si wafer (gray). b) SiO_2 (blue) is deposited a top the Si wafer with PECVD. c) Photoresist (red) is spin coated atop the oxidized wafer. d) UV light (arrows) is exposed through a patterned chrome mask (black) weakening the photoresist (pink). e) The weakened photoresist is removed, and the prepped wafer is now ready for etching.

Figure 2.2 - Diagram of the Preparation Step of the Chip Fabrication Process.

The etching process utilized consisted of two etching steps using Reactive-Ion Etching (RIE) with an Oxford Plasmalab 100 ICP RIE. RIE allows for etching through silicon and silicon based films to the nanometer precision (Sarifi and Gardner 2008). The first step was to etch through the thin SiO_2 film and expose the Si for the deep etching process. The recipe used (Table 2.2) allowed for good depth control and only etched the

wafer in areas where the photoresist was removed. After the first etching process, the photoresist was removed using a photoresist stripper (AZ400T), and the etching depth was confirmed using a Bruker Dektak XT Profiler. Measurement of the thickness of the SiO_2 film in areas not etched was also conducted in the same manner as previously to confirm its protection. The chip was then re-etched in the RIE with a recipe that selectively etched the exposed Si (Henry et al. 2009). This recipe can be viewed in **Table 2.3**. This allowed for deeper etching (micron level) in the areas of exposed Si while the areas with the SiO_2 were minimally etched. The depth of the channels were measured after this process again to confirm the target channel depth was reached. The SiO_2 film thickness was also measured again to confirm the selectivity. For the drilling step, the processed wafer was sent to an external company (Questech) for precision laser hole-drilling of the inlet/outlet ports. These steps, and the final bonding step, are presented in a diagram shown in **Figure 2.3**.

Table 2.2 - Etching Parameter Values for RIE of SiO_2.

Etch Parameter	**Value**	**Units**	**Etch Parameter**	**Value**	**Units**
Temperature	20.0	(Celsius)	**O_2**	5.0	(SCCM)
Pressure	45.0	(milliTorr)	**CHF_3**	45.0	(SCCM)
Forward Power	150	(Watts)	**Etch Rate**	~25.7	(nm/min)

Table 2.3 - Etching Parameter Values for RIE of Si

Etch Parameter	Value	Units	Etch Parameter	Value	Units
Temperature	-100.0	(Celsius)	**O_2**	8.0	(SCCM)
Pressure	10.0	(milliTorr)	**SF_6**	90.0	(SCCM)
Forward Power	5.0	(Watts)	**He**	38.0	(SCCM)
ICP	900	(Watts)	**Etch Rate**	~6.3	(μm/min)

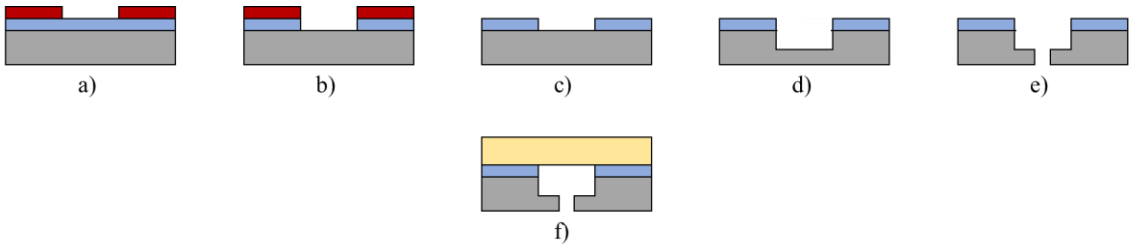

a) Process starts with the prepped Si wafer (gray). b) SiO_2 (blue) is etched using RIE through the pattern exposed by the photoresist (red), exposing the Si underneath. c) The photoresist is removed. d) RIE is used again to selectively etch the Si. e) Inlet/outlet ports are drilled into the etched wafer. f) A glass wafer (yellow) is bonded to the etched wafer, sealing and completing the microfluidic device.

Figure 2.3 - Diagram of the Etching, Drilling, and Bonding Steps for the Chip Fabrication Procedure.

The last step required for the fabrication of the microfluidic chip was to seal the chip by bonding a 2.2 mm borosilicate glass wafer (Borofloat 33) atop the processed silicon wafer. The purpose of this step is to seal the etched chamber network thus creating a microfluidic device that allows for fluids to be injected and pressurized within (Ouyang and Wang 2014). The use of borosilicate glass for the bonding allows for viewing of the fluids within the microfluidic device. Prior to bonding, the wafer and glass were cleaned

with piranha solution (3:1 mixture of sulfuric acid and 30% hydrogen peroxide). The bonding procedure was conducted using an EVG 501 Wafer Bonder and an anodic bonding recipe based on recommendations from Dziuban (2006). The anodic bonding recipe is shown in **Table 2.4**. The result of the bonding process was a complete microfluidic device with inlet and outlet ports. **Appendix B** includes various images and plots from the fabrication process.

Table 2.4 – Parameters Used for Anodic Bonding between a Processed Si Wafer and a Borosilicate Glass Wafer (2.2mm Thickness)

Bonding Parameter	Value	Units
Temperature	400.0	(Celsius)
Pressure	10.0	(milliTorr)
Voltage	1,000	(Volts)
Piston Force	1,500	(Newtons)

2.3. Experiment Setup and Procedure

A schematic for the setup used for experimentation can be seen in **Figure 2.4**. The experiment setup utilizes a custom made manifold to connect tubing to the microfluidic device, and secure the microfluidic device to the stage of a bottom viewing microscope (Leica DM IL LED). This allows for the experiment process to be viewed through the microscope software (Leica LAS X) while experiments are conducted. The top plate of

the manifold contains fixtures (Swagelok) that are placed above the inlet and outlet ports of the microfluidic device. An O-ring is placed around each of the ports, and the top plate is screwed into the stage manifold base to compress the O-ring thus creating a seal. There are two fixtures used for injection and one fixture used for vacuum. All connections are made using 1/16" stainless steel tubing (McMaster-Carr). One injection fixture is connected to a cylinder (High Pressure Equipment Co.) filled with the sample fluid. The other injection fixture is connected to a cylinder filled with a non-reactive and non-miscible fluid (with regards to the sample). This fluid will be used for pressurizing the sample fluid in the chambers. The fluid selected for use was ethylene glycol (99.8%). The outlet fixture is connected to a vacuum pump (Edwards).

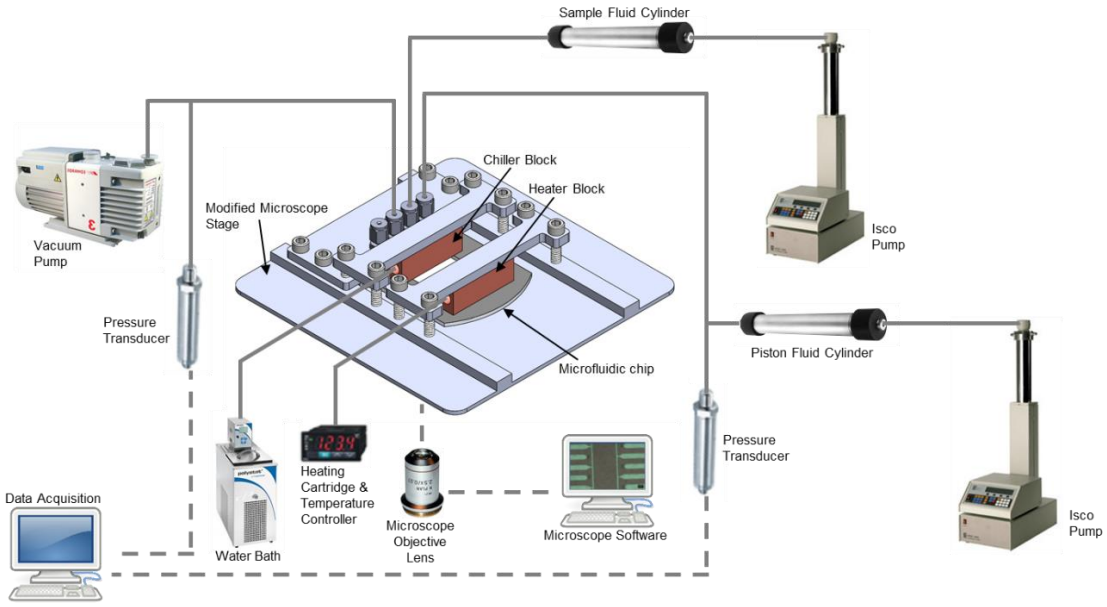

Figure 2.4 - Schematic of the Utilized Experiment Setup.

The experimental procedure is as follows. The device is first vacuumed. This will allow for the even flow of fluid throughout the device. The chambers are then uniformly filled with the sample fluid using the proper injection fixture. Then, a temperature gradient is applied across the rows using an external heating cartridge (Omega Engineering) and a cooling block connected to a circulating water bath (Cole-Parmer). A pressure gradient is applied from the inlet to outlet (down the column of rows) by injecting a pressurizing fluid using an ISCO pump (Teledyne Technologies) at the desired initial pressure. The vacuum pump is continuously used at the outlet to allow the pressurizing fluid to circulate throughout the system. This also allows for the setting of an outlet pressure. The inlet and outlet pressure applied by the pumps are measured by pressure transducers (Omega Engineering) and can be inferred as the upper and lower bounds of the applied pressure gradient, respectively. The system is allowed to stabilize, and images are captured of all the chambers using the microscope software. These images are then processed through an image analysis script to determine the phase of the sample (for a single component sample) or obtain relative volumes of liquid and gas (for a multi-component sample). Details on the image processing can be read in **Appendix A**. Using the observed pressure and temperature values at each chamber, a P-T diagram can then be created using the relative fluid volumes and phase boundaries observed.

3. EXPERIMENT RESULTS

3.1. Microfluidic Device Pressure Test

The purpose of this experiment was to determine the maximum pressure that could be contained within the microfluidic device before it failed.

Since this experiment was only testing the strength of the fabricated microfluidic device the experimental procedure was simplified from the previously described procedure by removing the sample injection step. So, this experiment consisted of vacuuming of the device, then the continuous injection of ethylene glycol to pressurize the system until the device failed. The injection rate started at 100 µL/min and was lowered to 20µL/min as the pressure was observed to be increasing very rapidly. The pressure was measured within the device during this process using a pressure transducer along the injection tubing.

3.1.1. Pressure Test Results

The results from the pressure test can be observed in **Figure 3.1**. This plot displays the pressure over time as the device was pressurized. A clear failure in the device is seen at the end of the experiment data where the pressure drops dramatically. From this plot, we observe that the maximum pressure the microfluidic device can withstand is about 975 psi.

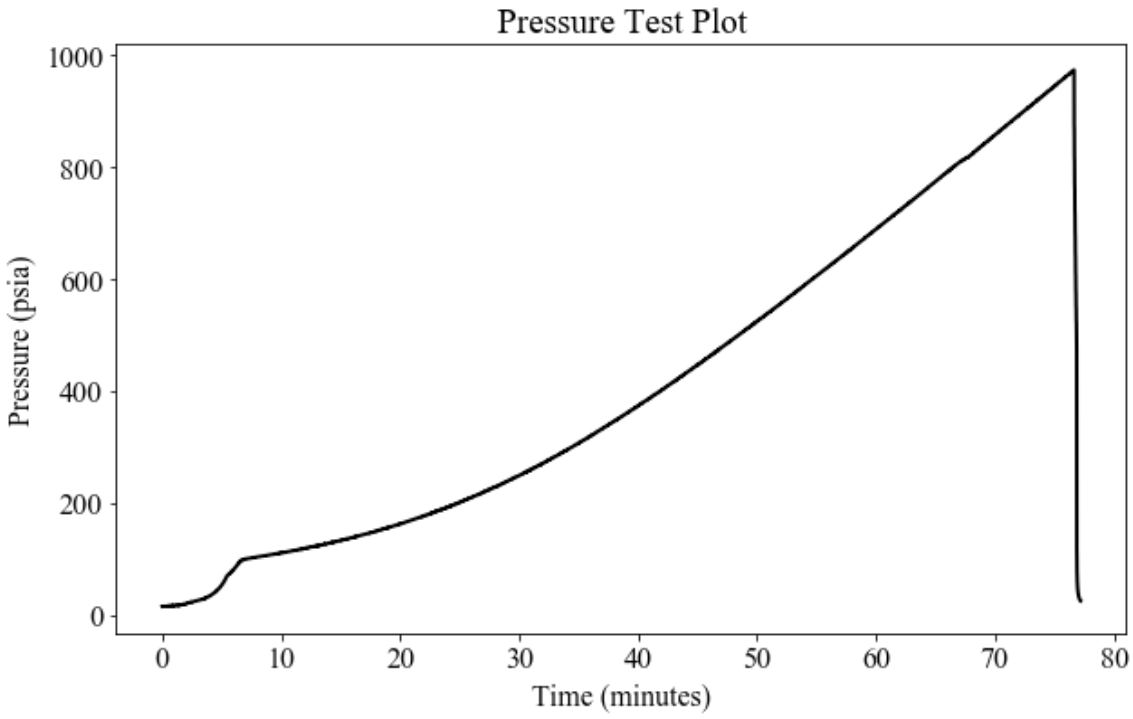

Figure 3.1 – Plot of Pressure vs. Time during the Pressure Test Displaying the Maximum Pressure the Device Can Withstand.

Looking at the device after the pressure test yields some useful information. **Figure 3.2** displays an image of the shattered microfluidic device after the pressure test experiment. The image shows that the failure of the device resulted in a clean break into four pieces. Seeing that the silicon wafer and borosilicate glass maintained their bond on each of the shattered pieces of the device, it can be deduced that the strength of the bond is greater than the failure pressure of one of the two wafers. The geometry of the fracture, combined with the observation that a thin layer of glass remained on the exposed silicon and the appearance of a visible crack within the borosilicate glass wafer, leads to the conclusion that the failure originated from the borosilicate glass wafer. **Figure 3.3**

displays two images of the fractured microfluidic device containing evidence that leads to the conclusion that the borosilicate glass wafer was the root of the device failure.

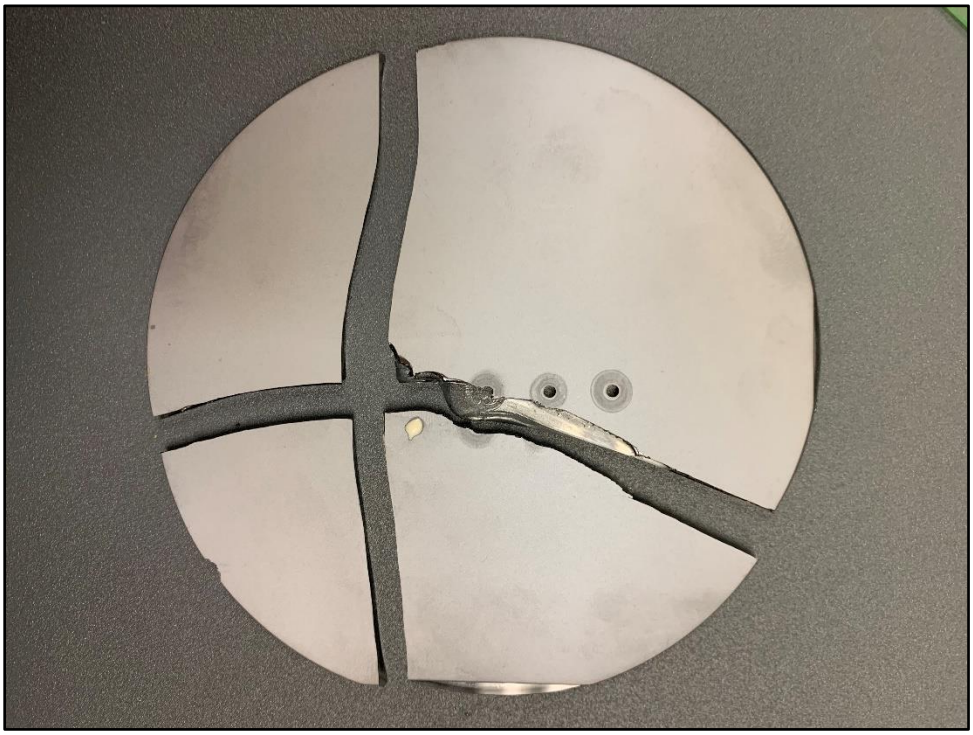

Figure 3.2 – Image of the Resulting Shattered Microfluidic Device after the Pressure Test Experiment.

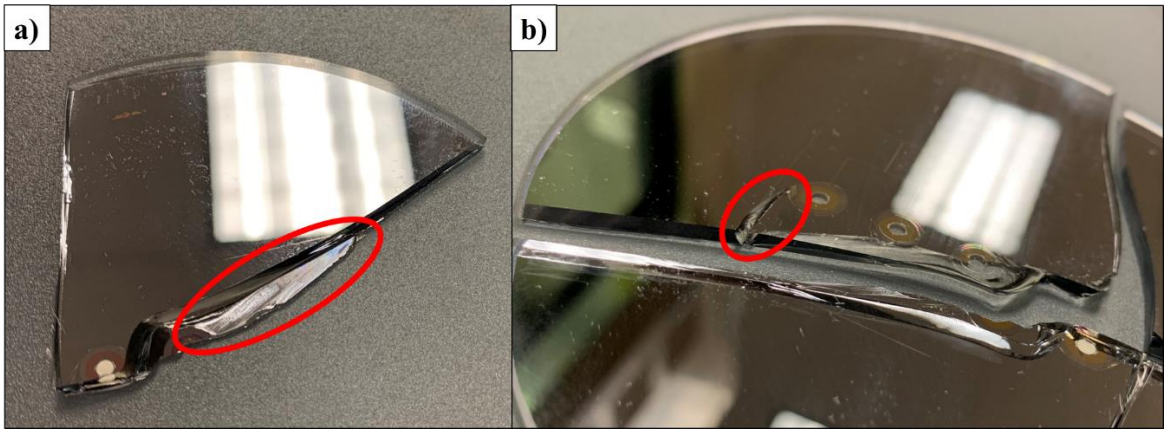

Figure 3.3 – a) Image Displaying a Visible Thin Film of Borosilicate Glass Remaining on the Exposed Silicon Wafer. b) A Visible Fracture in the Borosilicate Glass Wafer.

3.2. n-Butane P-T Diagram

To test the functionality of the microfluidic device and design as a means to generate PVT data, an experiment with a single component hydrocarbon was conducted. This experiment used n-butane (C_4H_{10}) as the sample fluid and followed the experimental procedure described previously. Due to the nature of n-butane regarding phase behavior, high pressure and high temperature gradients were not required to observe a significant portion of the P-T diagram. So, to not risk damage to the microfluidic device yet still yield substantial results, relatively low temperature and pressure gradients were utilized for this experiment. **Table 3.1** displays the temperature and pressure ranges that were applied during the experiment.

Table 3.1 – Temperature and Pressure Ranges Applied during the Experiment

Temperature	**Value**	**Units**	**Pressure**	**Value**	**Units**
Minimum	84.0	(Fahrenheit)	**Minimum**	17.0	(Psia)
Maximum	113.0	(Fahrenheit)	**Maximum**	69.0	(Psia)

3.2.1. n-Butane P-T Diagram Results

The raw images of each chamber were processed through the image analysis script, and each sample bubble was dyed with respects to the interpreted phase (green representing liquid and red representing gas). These processed chamber images were then compiled into a matrix and plotted against the applied pressure and temperature gradients to create a visual representation of the phase boundary. This visual can be seen in **Figure**

3.4. For this plot, seven of the ten rows of the chamber network were included. The phase was determined to be entirely gas within the rows that were not included, and thus, were omitted to allow a better view of the phase boundary.

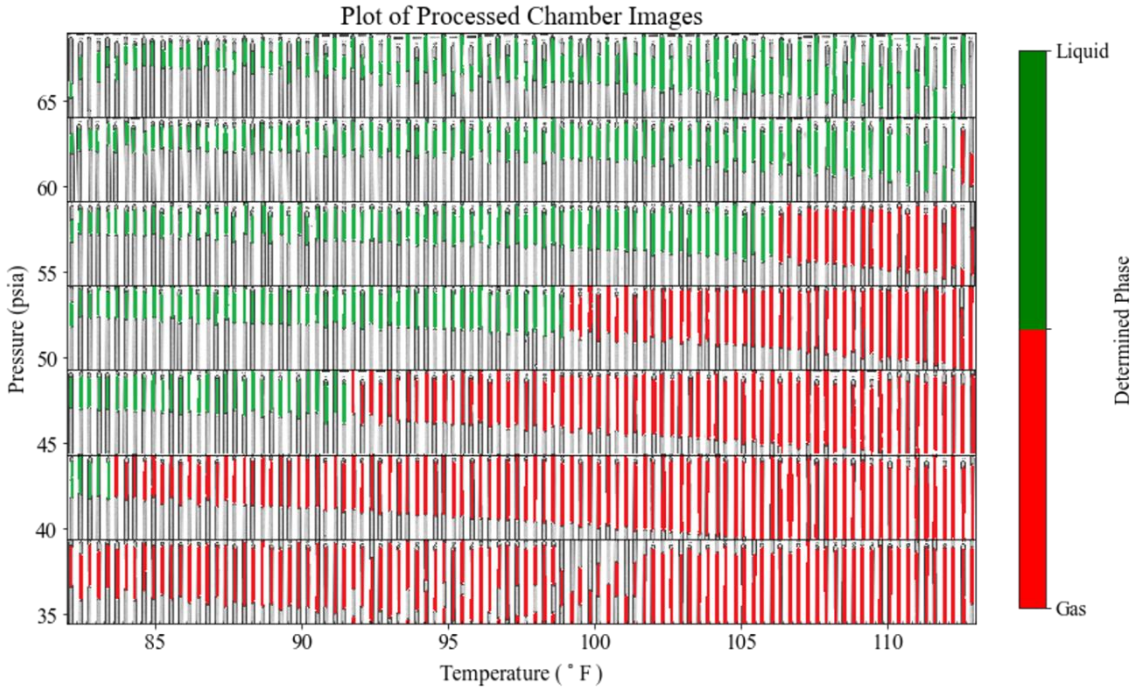

Figure 3.4 – Plot of the Processed Chamber Images Dyed to Indicate the Observed Phase (Green: Liquid, Red: Gas) within Each Chamber across Seven Pressure Steps, Displaying the Phase Boundary

A clearer visual representation of the same results obtained from the experiment is displayed in **Figure 3.5**. This plot displays a grid with each cell representing one of the microfluidic chambers within the device. Each of these cells is filled with a color that corresponds with the phase identified in that chamber (using the same color code as previously). The grid is also aligned with the applied pressure and temperature gradients to create a visual of the phase boundary, and the simulated P-T diagram across this range

of temperature and pressure was also included, obtained from WINPROP, to provide an assessment of the accuracy.

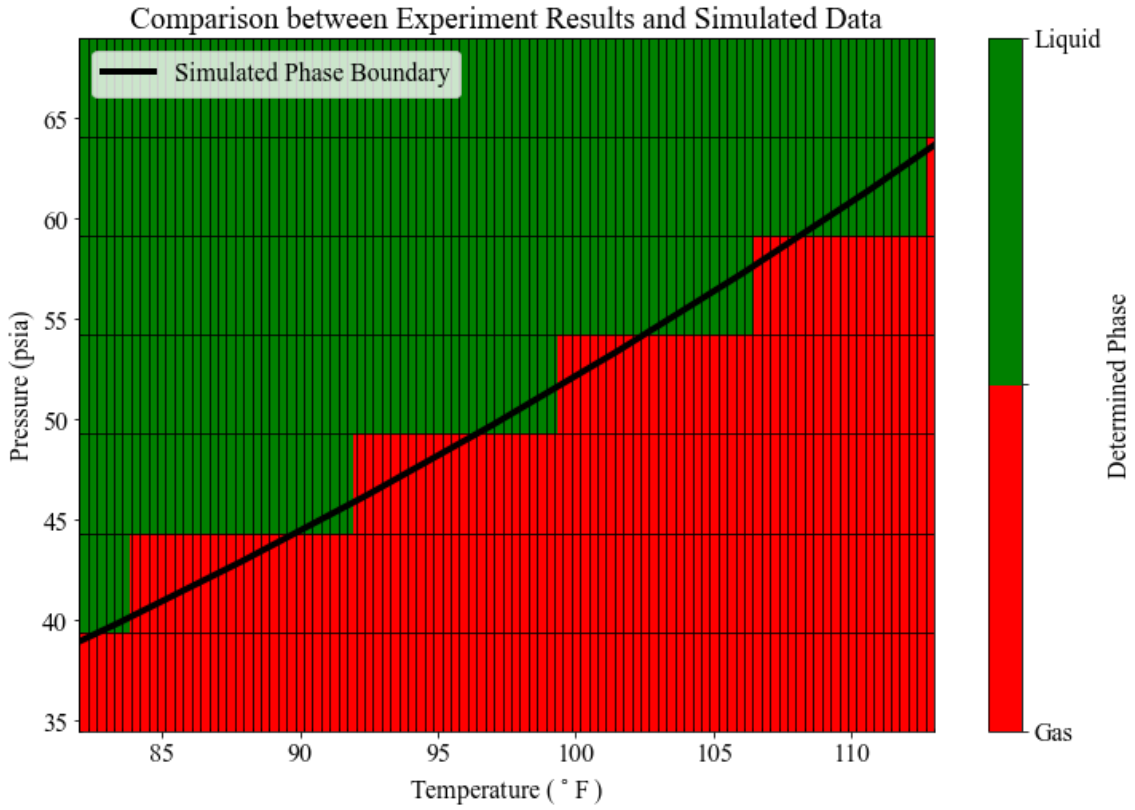

Figure 3.5 – A Visual Plot of the Observed Phase within Each Chamber across Seven Pressure Steps, Displaying the Phase Boundary

The visual presentation of the data shows that a phase boundary that follows the trend of the simulated data was observed. However, due to the few amount of pressure steps that can be utilized, this plot shows a rather coarse phase boundary for n-butane. To refine the boundary and generate a proper P-T diagram, the points where the phase changed were taken and plotted with their respective pressure and temperature then fit with a trend line. This plot along with the simulated data are displayed in **Figure 3.6**.

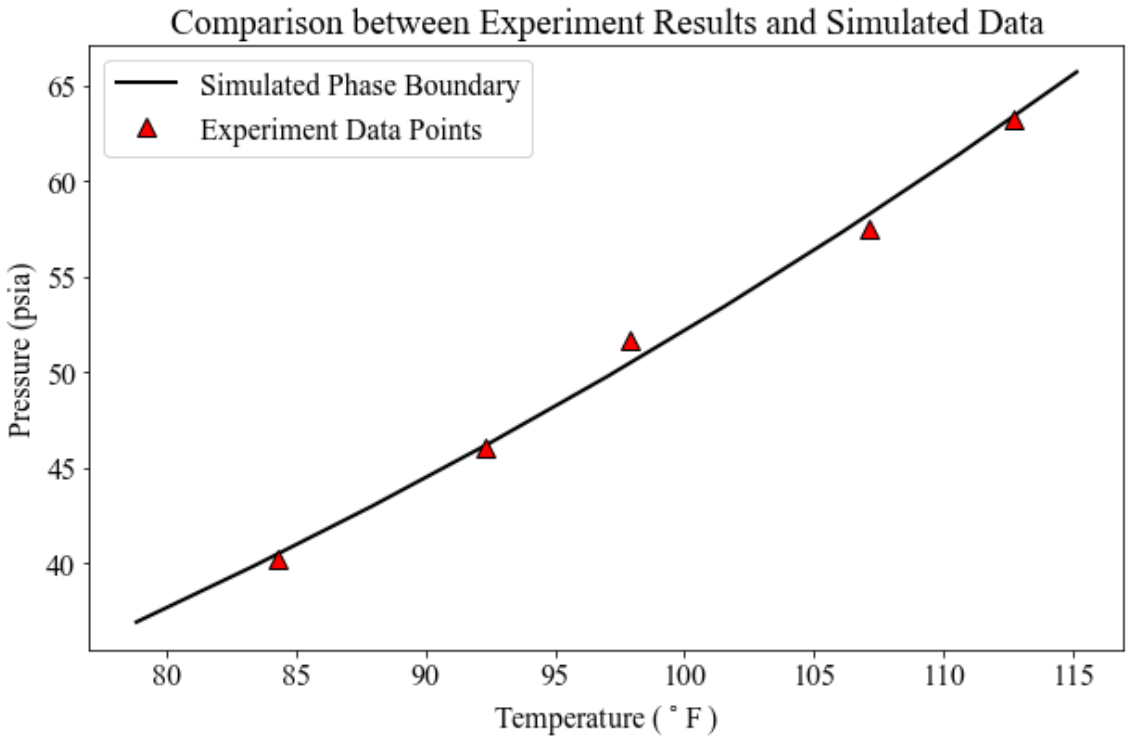

Figure 3.6 – Plot of the Phase Boundary Observed from the Experiment with a Power Law Trend Line and Including the Simulated Boundary for Comparison

The results show that over the observed temperature and pressure range, the created P-T diagram matches well with the simulated diagram. The average observed error between the experiment data and the simulated data is around 0.50%. This shows the validity of the experiment and its ability to reproduce simulated data.

To show the efficiency of the methodology, **Table 3.2** displays the total time required to conduct this experiment along with a breakdown of the time required to for each step of the procedure. Comparing the time required of around eight hours to the time required to conduct the same experiment using a PVT cell, around ten days, an order of magnitude reduction can be observed. When comparing the fluid volume required for the

experiment, the presented methodology uses roughly 4 mL of fluid, which is also an order of magnitude reduction when compared to the requirements of PVT cell experimentation (around 100 mL). These two reductions in time and volume of sample required lead to the presented experiment methodology being much more efficient than the currently utilized methodology while still maintaining the accuracy required.

Table 3.2 – Breakdown of the Time Required to Conduct the Experiment

Experiment Step	Time	Units
Vacuum Device	3.5	(Hours)
Fill with Sample	0.5	(Hours)
Pressure Up	3.0	(Hours)
Image Capture	1.25	(Hours)
Total	8.25	(Hours)

4. CONCLUSIONS AND FUTURE WORK

4.1. Conclusion

Current methodologies used for generating P-T diagrams are time-consuming and expensive. A microfluidic approach to generating P-T diagrams through the use of a device that simultaneously heats and pressurizes of 1,000 microfluidic chambers to obtain CCE data points is shown to provide a valid alternative.

The methodology for fabricating the microfluidic devices utilized is shown to produce microfluidic devices capable of withstanding close to 1,000 psi. The methodology is detailed enough to serve as a blueprint for the fabrication of other silicon-glass microfluidic devices

The experiment performed on n-butane demonstrates that the microfluidic device design and experimental procedure are capable of producing a P-T diagram with an error of around 0.50% over the applied pressure and temperature range. The experiment was able to produce these results in a fraction of the time required to produce similar results with PVT cell experimentation while using a fraction of the fluid as well.

4.2. Future Work

Though the demonstrated results show the validity of the experiment methodology, further experimentation should be conducted. Using the same microfluidic device design, an experiment using a multi-component hydrocarbon sample should be conducted to demonstrate the device's capability to create a visual 2-phase envelope that can be interpreted into an accurate P-T diagram. If successful, the device should be further tested

using an actual field gas sample to demonstrate the applicability of this device with real-world samples.

Though the fabricated device is shown to withstand pressures that can generate full P-T diagrams for most hydrocarbons, the improvement of the fabrication process to withstand even higher pressures would be valuable. Since the failure of the device was observed to be due to the borosilicate glass wafer, a thicker glass wafer should be a simple change to improve the pressure rating of the microfluidic devices. Experiments utilizing increased thicknesses of borosilicate glass should be conducted to determine if bonding to the silicon substrate is possible and to understand the correlation between the thickness of the borosilicate glass wafer and the maximum pressure the fabricated microfluidic device can withstand.

Lastly, it would be of interest to reduce the scale of this device design to the nanoscale. If experimentation was conducted with this design in the nanoscale, it could provide valuable information with regards to confinement effects on the P-T diagram. It is known hydrocarbon gas phase behavior is altered when confined to channels in the nanoscale, but a full P-T diagram has yet to be investigated at this scale. Conducting this experiment could provide insight on the phase behavior of hydrocarbons when confined within tight unconventional plays.

REFERENCES

Alfi, M., Banerjee, D., and Nasrabadi, H. 2016a. Effect of Confinement on the Dynamic Contact Angle of Hydrocarbons, *Energy Fuels* **30**: 8962–8967.

Alfi, M., Banerjee, D., and Nasrabadi, H. 2016b. Experimental Investigation of Confinement Effect on Phase Behavior of Hexane, Heptane and Octane Using Lab-on-a-Chip Technology, *Fluid Phase Equilib.* **423**: 25–33.

Alfi, M., Nasrabadi, H., and Banerjee, D. 2017. Effect of Confinement on Bubble Point Temperature Shift of Hydrocarbon Mixtures: Experimental Investigation Using Nanofluidic Devices. Paper presented at the SPE Annual Technical Conference and Exhibition, San Antonio, Texas, USA, 9–11 October. SPE-187057-MS.

Armstrong, R. T., and Wildenschild, D. 2012. Investigating the Pore-Scale Mechanisms of Microbial Enhanced Oil Recovery, *J. Pet. Technol.* **94-95**: 155–164.

Bao, B., Riordan, J., and Mostowfi, F. et al. 2017. Microfluidic and Nanofluidic Phase Behaviour Characterization for Industrial CO2, Oil and Gas, *Lab Chip* **17**: 2740–2759.

Bao, B., Riordon, J., and Xu, Y. et al. 2016. Direct Measurement of the Fluid Phase Diagram, *Anal. Chem.* **88**: 6986–6989.

Berejnov, V., Djilali, N., and Sinton, D. 2008. Lab-on-Chip Methodologies for the Study of Transport in Porous Media: Energy Applications, *Lab Chip* **8**: 689–693.

Bonnet, J., and R. Lenormand. 1977. Realisation de-micromodeles pour l'etude des ecoluments polyphasiques en milieu poreux, *Rev. Inst. Fr. Pet.* **42**:477–480.

Bowden, S. A., Cooper, J.M., and Greub, F. et al. 2010. Benchmarking Methods of Enhanced Heavy Oil Recovery Using a Microscaled Bead-Pack, *Lab Chip* **10**: 819–823.

Bowden, S. A., Wilson, R., and Parnell, J. et al. 2009. Determination of the Asphaltene and Carboxylic Acid Content of a Heavy Oil Using a Microfluidic Device, *Lab Chip* **9**: 828–832.

Buchgraber, M., Clemens, T., and Castanier, L.M. et al. 2011. A Microvisual Study of the Displacement of Viscous Oil by Polymer Solutions, *SPE Reservoir Eval. Eng.* **14** (3): 269–280.

De Haas, T. W., Fadaei, H., and Guerrero, U. et al. 2013. Steam-on-a-Chip for Oil Recovery: The Role of Alkaline Additives in Steam Assisted Gravity Drainage, *Lab Chip* **13**: 3832–3839.

Di Primio, R., Dieckmann, V., and Mills, N. 1998. PVT and Phase Behaviour Analysis in Petroleum Exploration, *Organic Geochemistry* **29** (1-3): 207–222.

Dzubian, J. A. 2006. *Bonding in Microsystem Technology*, Berlin, Germany: Springer.

Fadaei, H., Scarff, B., and Sinton, D. 2011. Rapid Microfluidics-Based Measurement of CO_2 Diffusivity in Bitumen, *Energy Fuels* **25**: 4829–4835.

Fadaei, H., Shaw, J. M., and Sinton, D. 2013. Bitumen–Toluene Mutual Diffusion Coefficients Using Microfluidics, *Energy Fuels* **27**: 2042–2048.

Firoozabadi, A. 1999. *Thermodynamics of Hydrocarbon Reservoirs*, first edition, New York City, NY: McGraw-Hill Education.

Gale, B. K., Jafek, A. R., and Lambert, C. J. et al. 2018. A Review of Current Methods in Microfluidic Device Fabrication and Future Commercialization Prospects, *Inventions* **3** (3): 60.

Gunda, N. S. K., Bera, B., and Karadimitriou, N. K. et al. 2011. Reservoir-on-a-Chip (ROC): A New Paradigm in Reservoir Engineering, *Lab Chip* **11**: 3785–3792.

Günther, A., and Jensen, K. F. 2006. Multiphase Microfluidics: From Flow Characteristics to Chemical and Materials Synthesis, *Lab Chip* **6**: 1487–1503.

Harriott, L. R. 2001. Limits of Lithography, *Proceedings of the IEEE* **89** (3): 366–371.

Henry, M. D., Welch, C., and Scherer, A. 2009. Techniques of Cryogenic Reactive Ion Etching in Silicon for Fabrication of Sensors, *J. Vac. Sci. Technolog. A* **27** (5): 1211–1216.

Jin, B., Bi, R., and Nasrabadi, H. 2017. Molecular Simulation of the Pore Size Distribution Effect on Phase Behavior of Methane Confined in Nanopores, *Fluid Phase Equilibria* **452**: 94–102.

Jin, Z., Firoozabadi, A. 2015. Flow of Methane in Shale Nanopores at Low and High Pressure by Molecular Dynamics Simulations, *J. Chem. Phys.* **143**: 104315.

Keck Microfabrication Facility. 2002. SOP – Photoresist Processing. Iowa State University, Ames, Iowa.

Khajepour, H., Mahmoodi, M., and Biria, D. et al. 2014. Investigation of Wettability Alteration through Relative Permeability Measurement during MEOR Process: A Micromodel Study, *J. Pet. Technol.* **120**: 10–17.

Kuila, U., and Prasad, M. 2013. Specific Surface Area and Pore-Size Distribution in Clays and Shales, *Geophysical Prospecting* **61**: 341–362.

Lifton, V. A. 2016. Microfluidics: An Enabling Screening Technology for Enhanced Oil Recovery (EOR), *Lab Chip* **16**: 1777–1796.

Luo, S., Lutkenhaus, J. L., and Nasrabadi, H. 2017. Multi-Scale Fluid Phase Behavior Simulation in Shale Reservoirs by a Pore-Size-Dependent Equation of State. Paper presented at the SPE Annual Technical Conference and Exhibition, San Antonio, Texas, USA, 9–11 October. SPE-187422-MS.

Luo, S., Lutkenhaus, J. L., and Nasrabadi, H. 2018. Use of Differential Scanning Calorimetry to Study Phase Behavior of Hydrocarbon Mixtures in Nano-Scale Porous Media, *Journal of Petroleum Science and Engineering* **163**: 731–738.

Luo, S., Nasrabadi, H., and Lutkenhaus, J. L. 2016. Effect of Confinement on the Bubble Points of Hydrocarbons in Nanoporous Media, *AIChE Journal* **62** (5): 1772–1780.

Luther, S. K., Schuster, J. J., and Leipertz, A. et al. 2013. Microfluidic Investigation into Mass Transfer in Compressible Multi-Phase Systems Composed of Oil, Water, and Carbon Dioxide at Elevated Pressure, *J. of Supercrit. Fluids* **84**: 121–131.

Luther, S. K., Stehle, S., and Weihs, K. et al. 2015. Determination of Vapor – Liquid Equilibrium Data in Microfluidic Segmented Flows at Elevated Pressures Using Raman Spectroscopy, *Anal. Chem.* **87**: 8165–8172.

Ma, S., Murphy, T.W., and Lu, C. 2017. Microfluidics for Genome-Wide Studies Involving Next Generation Sequencing, *Biomicrofluidics* **11** (2): 021501.

Manz, A., Graber, N., and Widmer, H.M. 1990. Miniaturized Total Chemical Analysis Systems: a Novel Concept for Chemical Sensing, *Sensors and Actuators* **B1**: 244–248.

Marre, S., Adamo, A., and Basak, S. et al. 2010. Design and Packaging of Microreactors for High Pressure and High Temperature Applications, *Ind. Eng. Chem. Res.* **49**: 11310–11320.

Marshall, A., and Hodgson, J. 1998. DNA Chips: An Array of Possibilities, *Nature Biotechnology* **16**: 27–31.

McCain, W.D. 1990. *The Properties of Petroleum Fluids*, second edition. Tulsa, OK: PennWell.

Metzler, M., and Patel, R. 2017. Plasma Enhanced Chemical Vapor Deposition (PECVD) of Silicon Dioxide (SiO2) Using Oxford Instruments System 100 PECVD, *Tool Data* **34**.

Meybodi, H. E., Kharrat, R., and Wang, X. 2011. Study of Microscopic and Macroscopic Displacement Behaviors of Polymer Solution in Water-Wet and Oil-Wet Media, *Transp. Porous Med.* **89**: 97–120.

Molla, S., Magro, L., and Mostowfi, F. 2016. Microfluidic Technique for Measuring Wax Appearance Temperature of Reservoir Fluids, *Lab Chip* **16**: 3795–3803.

Mora, M. F., Greer, F., and Stockton, A. M. et al. 2011. Toward Total Automation of Microfluidics for Extraterrestial In Situ Analysis, *Anal. Chem.* **83**: 8636–8641.

Mostowfi, F., Molla, S., and Tabeling, P. 2012. Determining Phase Diagrams of Gas-Liquid Systems Using a Microfluidic PVT, *Lab Chip* **12**: 4381–4387.

Nge, P., Rogers, C., and Woolley, A. 2013. Advances in Microfluidic Materials, Functions, Integration, and Application, *Chem. Rev.* **113**: 2550–2583.

Nguyen, P., Mohaddes, D., and Riordon, J. et al. 2015. Fast Fluorescence-Based Microfluidic Method for Measuring Minimum Miscibility Pressure of CO_2 in Crude Oils, *Anal. Chem.* **87**: 3160–3164.

Nguyen, N.T., Wereley, S.T., and Shaegh, S.A.M. 2019. *Fundamentals and Applications of Microfluidics*, third edition. Norwood, MA: Artech House.

Oren, P. E., and Pinczewski, W.V. 1995. Fluid Distribution and Pore-Scale Displacement Mechanisms in Drainage Dominated Three-Phase Flow, *Transport in Porous Media* **20**: 105–133.

Ouyang, W., and Wang, W. 2014. Fabrication and Characterization of Sub-100/10 nm Planar Nanofluidic Channels by Triple Thermal Oxidation and Silicon-Glass Anodic Bonding, *Biomicrofluidics* **8**: 052106

Parsa, E., Yin, X., and Ozkan, E. 2015. Direct Observation of the Impact of Nanopore Confinement on Petroleum Gas Condensation. Paper presented at the SPE Annual Technical Conference and Exhibition held in Houston, Texas, USA, 28–30 September 2015. SPE-175118-MS.

Pinho, B., Girardon, S., and Bazer-Bachi, F. et al. 2014. A Microfluidic Approach for Investigating Multicomponent System Thermodynamics at High Pressures and Temperatures, *Lab Chip* **14**: 3843–3849.

Reedy, C. R., Hagan, K. A, and Strachan, B. C. et al. 2010. Dual-Domain Microchip-Based Process for Volume Reduction Solid Phase Extraction of Nucleic Acids from Dilute, Large Volume Biological Samples, *Anal. Chem.* **82**: 5669–5678.

Reyes, D., Iossifidis, D., and Auroux, P. et al. 2002. Micro Total Analysis Systems. 1. Introduction, Theory, and Technology, *Anal. Chem.* **74**: 2623-2636.

Sanders, G.H.W., and Manz, A. 2000. Chip-Based Microsystems for Genomic and Proteomic Analysis, *Trends in Analytical Chemistry* **19** (6): 364–378.

Sharifi, H., and Gardner, G. 2008. Plasma RIE Etching Fundamentals and Applications. Lecture, Purdue University, West Lafayette, Indiana.

Sinton, D. 2014. Energy: The Microfluidic Frontier, *Lab Chip* **14**: 3127–3134.

Sohrabi, M., Danesh, A., and Jamiolahmady, M. 2008. Visualisation of Residual Oil Recovery by Near-Miscible Gas and SWAG Injection Using High-Pressure Micromodels, *Transp. Porous Med.* **74**: 239–257.

Sullivan, M. T., and Angelescu, D. E. 2016. Microfluidic Bubble Point Measurement Using Thermal Nucleation, *Energy Fuels* **30**: 2655–2661.

Terry, S., Jerman, J., and Angell, J. 1979. A Gas Chromatographic Air Analyzer Fabricated on a Silicon Wafer, *IEEE Transactions on Electron Devices* **26** (12): 1880–1886.

Togo, M., Maeda, T., and Ito, A. et al. 2013. Measurement and Correlation of Phase Equilibria for (Water + Aromatic Hydrocarbon) Binary Mixtures at T = (573 to 623) K Using Microfluidic Mixing, *J. Chem. Thermodynamics* **67**: 247–252.

Wang, L., Parsa, E., and Gao, Y. et al. 2014. Experimental Study and Modeling of the Effect of Nanoconfinement on Hydrocarbon Phase Behavior in Unconventional Reservoirs. Paper presented at the SPE Western North American and Rocky

Mountain Joint Regional Meeting held in Denver, Colorado, USA, 16–18 April, 2014. SPE-169581-MS.

Whitesides, G. 2006. The Origins and the Future of Microfluidics, *NATURE* 442: 368–373.

Whitson, C.H. and Brulé, M.R. 2000. *Phase Behavior*, No. 20. Richardson, TX: Henry L. Doherty Monograph Series, Society of Petroleum Engineers.

Xu, Y., Riordon, J., and Cheng, X. et al. 2017. The Full Pressure-Temperature Phase Envelope of a Mixture in 1000 Microfluidic Chambers, *Angew. Chem. Int. Ed.* **56** (45): 13962–13967.

Yang, Q., Jin, B., and Banerjee, D. et al. 2019. Direct Visualization and Molecular Simulation of Dewpoint Pressure of a Confined Fluid in Sub-10 nm Slit Pores, *Fuel* **235**: 1216–1223.

APPENDIX A

The results of conducting the experiment are a series of photographs of each chamber of the microfluidic device. These images are captured using contrast and saturation settings that emphasize the difference between the gas phase and liquid phase of the fluid sample and also show a clear boundary between the ethylene glycol and the sample. An example of one of these images can be viewed in **Figure A.1**.

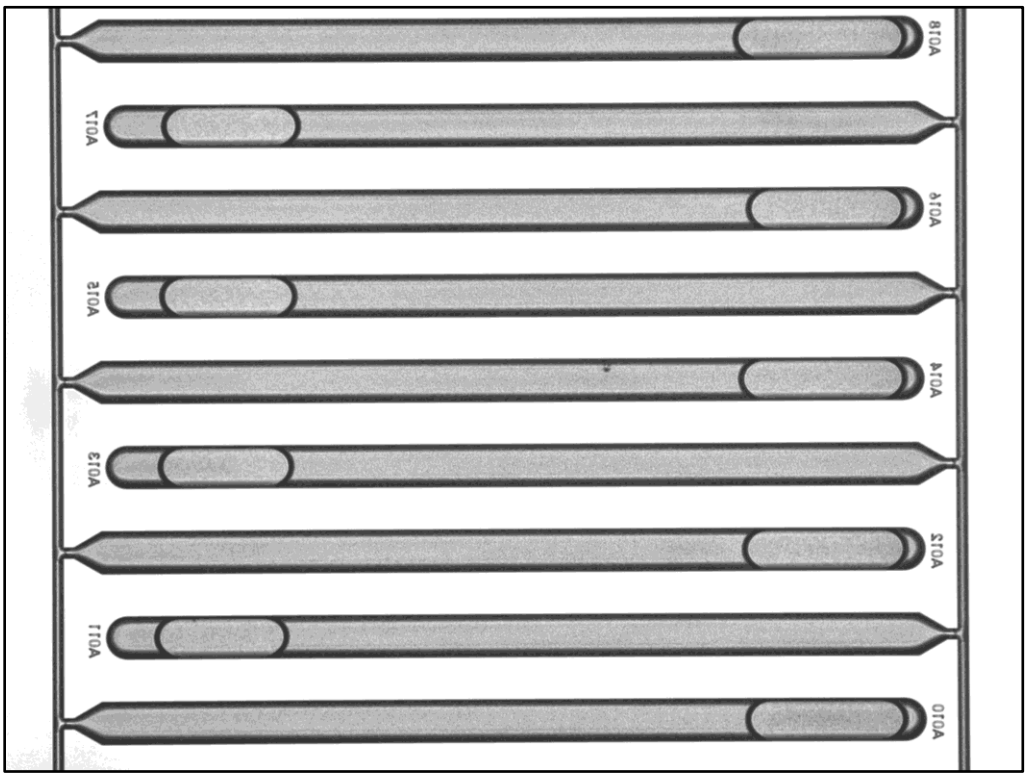

Figure A.1 – Sample Raw Image Capture from the Conducted Experiment

To process these raw captured images, the images were first cropped to divide the chambers to individual images using a python script. The process of analyzing the individual chambers depends on the sample itself. If it is a single-component or multi-component hydrocarbon. The reason for this is that for single-component samples, the

sample is a single phase within each chamber, and for multi-component samples, the chambers may contain two phases.

Single-Component Sample Analysis

The objective of analysis for a single component sample is to determine if the sample is liquid or gas within each chamber. To identify the difference, comparisons between chambers where the sample is known to be liquid and gas were made. Known liquid and gas examples can be selected based on the applied pressure and temperature gradients. **Figure A.2** displays a comparison of two chambers at the same temperature but on opposite ends of the pressure range, highlighting the difference between the liquid and gas phases. **Figure A.3** displays a comparison of two chambers at the same pressure but on opposite ends of the temperature range, also displaying the difference between the liquid and gas phases.

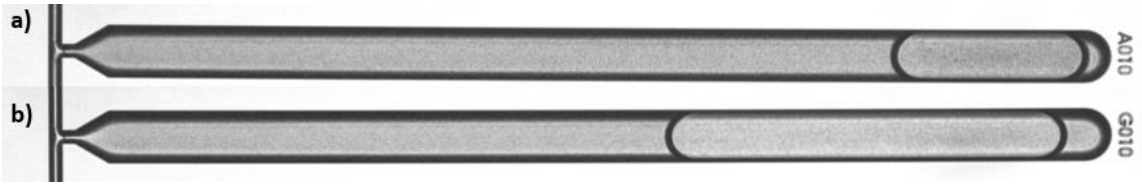

Figure A.2 – a) Chamber A010 (Higher Pressure) Displays the Liquid Phase.
b) Chamber G010 (Lower Pressure) Displays the Gas Phase.

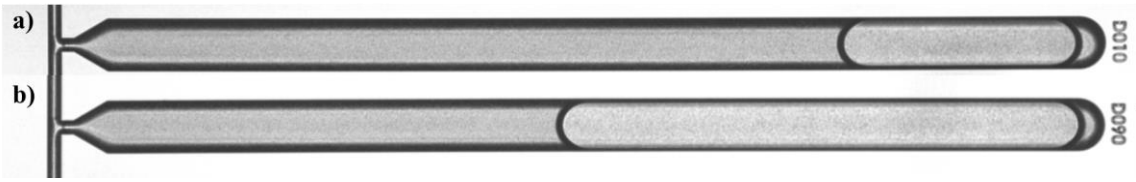

Figure A.3 – a) Chamber D010 (lower temperature) Displays the Liquid Phase.
b) Chamber D090 (Higher Temperature) Displays the Gas Phase

Using the differences noted as temperature and pressure change, cut-offs based on the color and size of the sample bubble were used to determine the phase. This process was semi-automated and required some interpretation.

Multi-Component Sample

Though the experimentation has not been conducted, an image analysis script was generated for the interpretation of the raw image data for a multi-component sample. The objective when interpreting the results for a multi-component sample is to determine the relative volume of liquid and gas within each chamber where two phases are observed. A sample image obtained from Xu et al. (2017) was used for the generation of the script. The script uses canny edge detection to identify the fluid bubbles and then compute the relative volumes based on the number of pixels each bubble occupies. **Figure A.4** displays a visual of the steps in this process. The determination of which bubble is liquid and which bubble is gas is made based on the position of the chamber relative to where single phase is observed. So, if the chamber is close to the bubble point line, then the larger bubble should be the liquid phase.

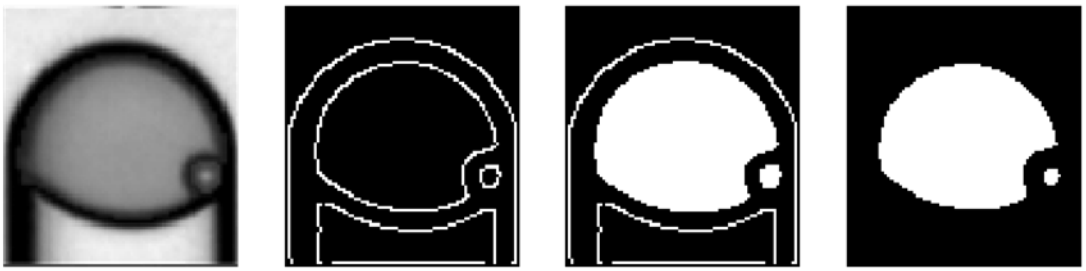

Figure A.4 – Steps for the Two-Phase Image Analysis Process

APPENDIX B

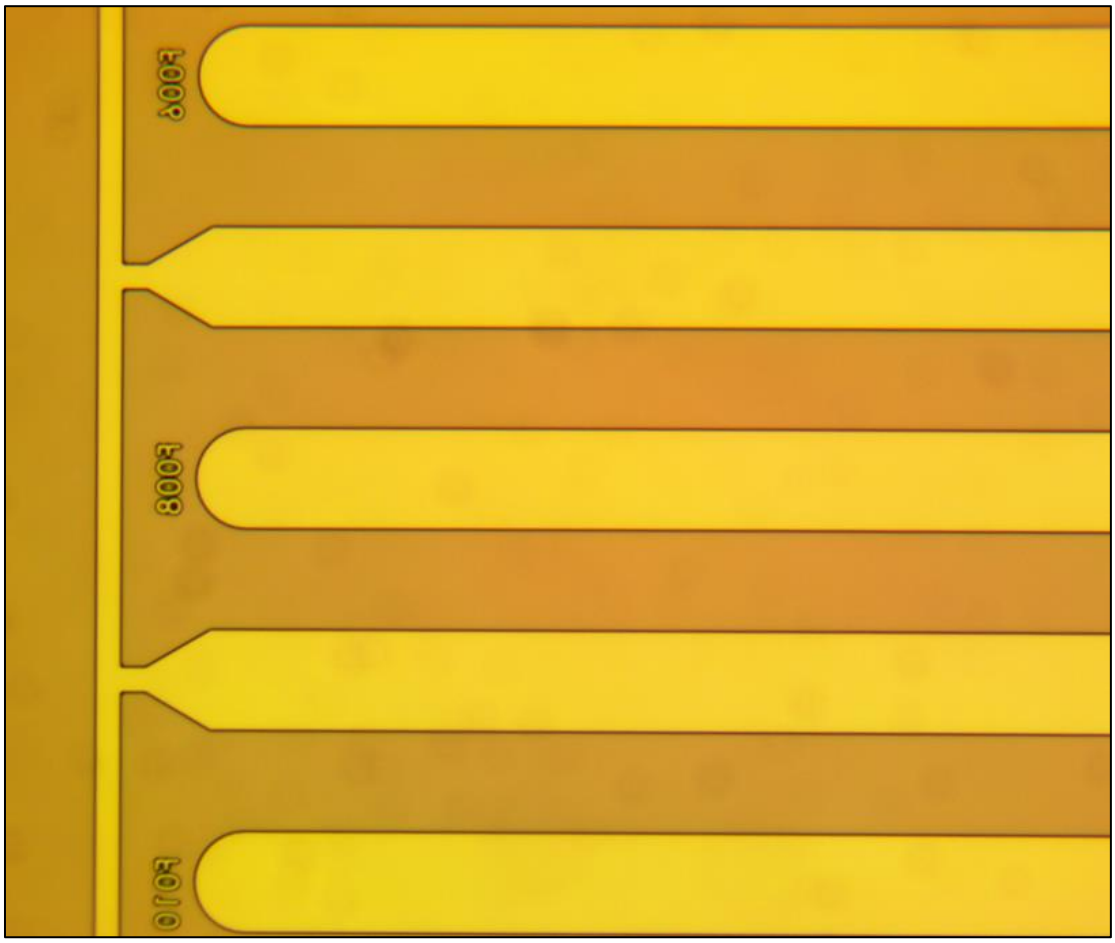

Figure B.1 – 5x Microscope Image of a Wafer after Spin Coating and Lithography Displaying the Design Developed onto the Wafer.

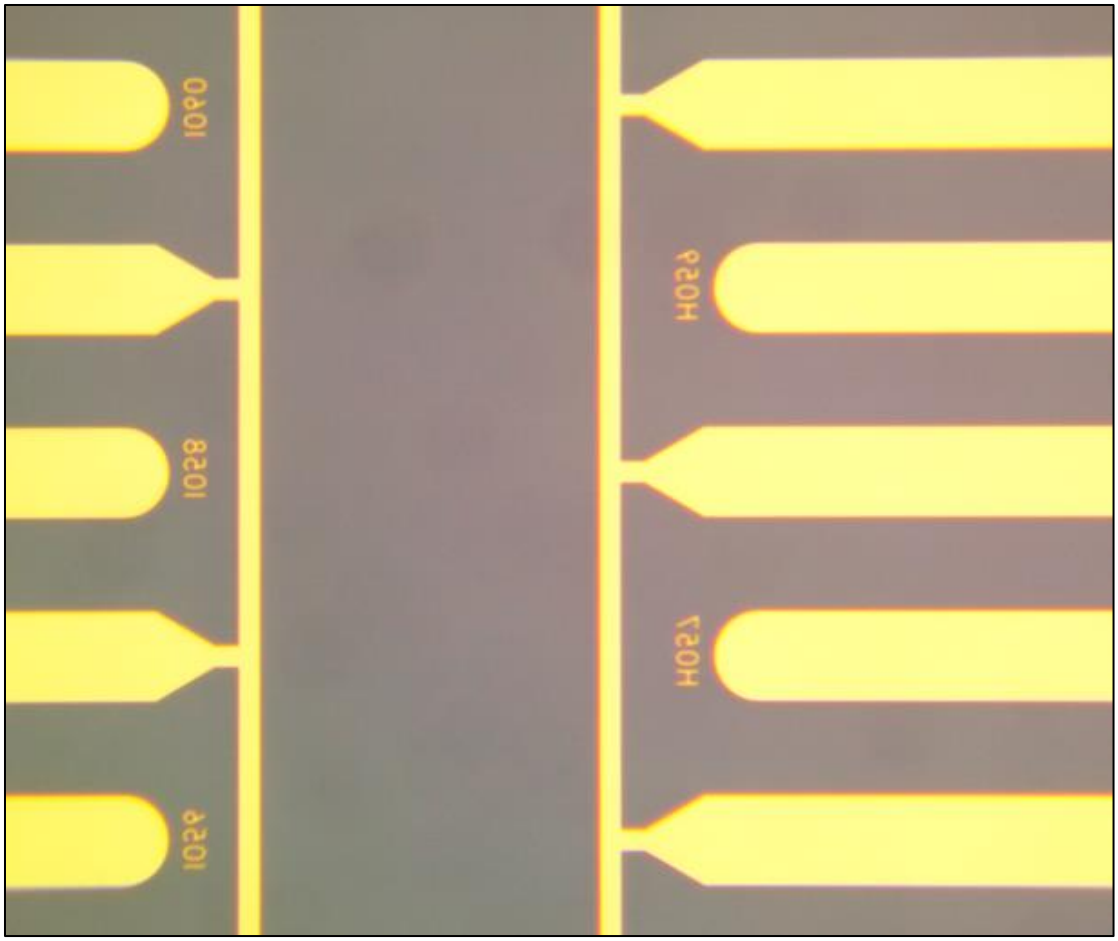

Figure B.2 – 5x Microscope Image of a Wafer after the First Etching Step, Displaying the Design Etched through the Silicon Dioxide and Exposing the Silicon.

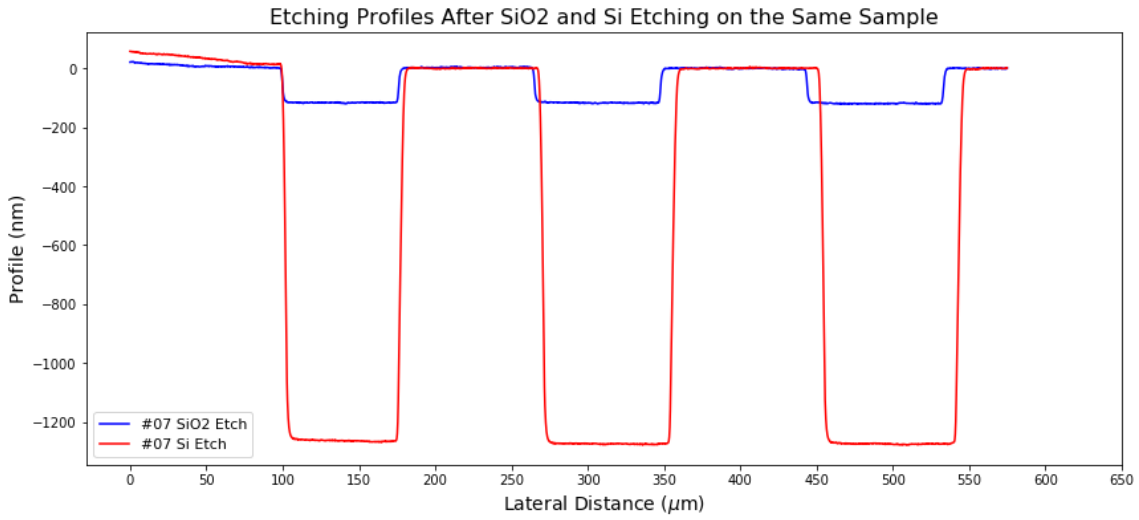

Figure B.3 – Plot of the Profiles Measured across 3 Chambers using a Dektak XT Profiler. The Blue Curve Displays the Measurement after the SiO_2 Etching and the Red Curve Displays the Measurement after the Si Etching.

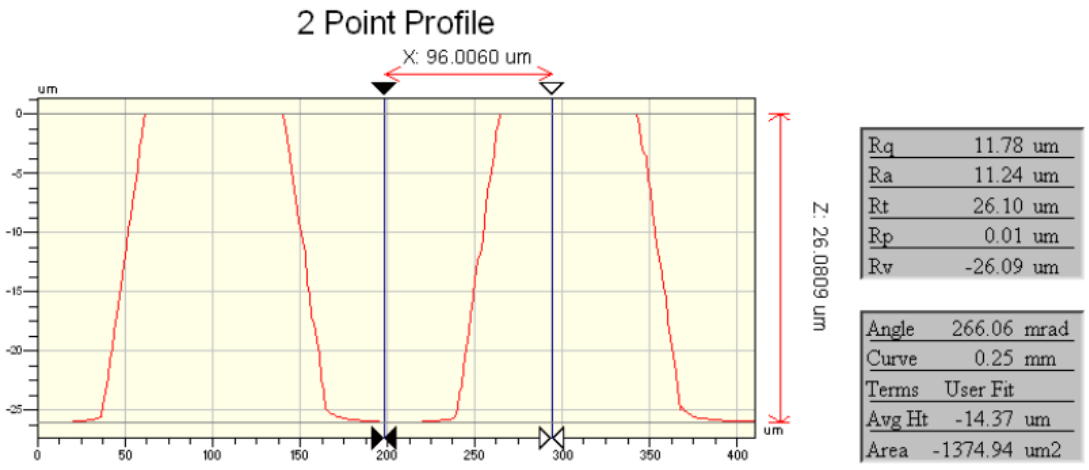

Figure B.4 – Plot of the Profile Measured across 2 Chambers using a Veeco Optical Profilometer. The Measurement was Conducted after the Si Etching.